Polymer Aggregates

International Edition: DOI: 10.1002/anie.201710336
German Edition: DOI: 10.1002/ange.201710336

In Situ Optical Imaging of the Growth of Conjugated Polymer Aggregates

*Jaesung Yang, Heungman Park, and Laura J. Kaufman**

Abstract: *Understanding the mechanisms that contribute to conjugated polymer aggregate formation and growth may yield enhanced control of aggregate morphology and functional properties on the mesoscopic scale. In situ optical imaging of the growth of MEH-PPV aggregates in real time in controlled swollen films shows that growth occurs through multiple mechanisms and is more complex than previously described. Direct evidence is provided for both Ostwald ripening and aggregate coalescence as operative modes of aggregate growth in solvent swollen films. These growth mechanisms have a distinct and strong impact on the evolution of morphological order of growing aggregates: while Ostwald ripening allows preservation of highly ordered morphology, aggregate coalescence occurs with no preferential orientation, leading to attenuation in degree of ordering.*

Mesoscopic aggregates of conjugated polymers play a crucial role in determining the performance of organic thin film devices. Indeed, numerous studies on bulk films have demonstrated that aggregate morphology is very strongly associated with charge-transport properties.[1] However, a microscopic understanding of the impact of aggregate morphology has proven difficult to attain since bulk films contain domains with disparate levels of organization from amorphous to highly ordered, each of which may span a variety of length scales.

Solvent vapor annealing (SVA) of thin films containing dispersed single conjugated polymers in inert host polymer matrices offers a unique opportunity to prepare conjugated polymer aggregates through bottom-up assembly and interrogate them on an individual basis with established single particle techniques. Already, research employing SVA has informed understanding of the relationships between single polymer and mesoscopic aggregate morphology and exciton transport behavior.[2]

Despite the emergence of SVA as a technique that allows controlled preparation of individual aggregates, the growth mechanism of these aggregates is incompletely understood. One previous study provided evidence that conjugated polymer aggregation occurs via Ostwald ripening,[2a,3] a thermodynamic process in which larger aggregates grow at the expense of smaller ones through single molecule transfer. However, no real time experimental observation supporting this conclusion has been described. As such, it remains unclear whether Ostwald ripening is an operative mechanism in aggregate growth in swollen films and whether other growth mechanisms such as particle coalescence, as substantially evidenced in nanocrystal growth, also play a role.[4] Furthermore, it is not known if and how aggregate growth mechanism impacts aggregate morphology and functional properties, and therefore whether control of growth mechanism may allow fine tuning of these properties. In situ observation of aggregation can address many of these questions. One obstacle limiting in situ real-time interrogation of aggregate growth is intimately related to the process itself, in which significant mobility of isolated entities is required. In conventional SVA experiments, the extent of film swelling is such that aggregate diffusion is too fast for adequate localization and characterization of aggregates. To circumvent this problem, we developed an SVA chamber that allows in situ monitoring of film swelling on a quartz crystal microbalance (QCM) while performing optical imaging of an equivalent film on the chamber bottom.[2j] This experimental setup allows control and monitoring of the degree of film swelling, allowing control of particle speed for in situ tracking and interrogation of individual aggregates during the growth process.

Using this approach, we show that multiple growth mechanisms are at play during the growth of conjugated polymer aggregates and that aggregate growth does not proceed solely through Ostwald ripening. By performing quasi real-time polarization anisotropy experiments and complementary Monte Carlo simulations, we also demonstrate that particular growth mechanisms critically impact morphological order of growing aggregates.

Aggregates were prepared from the paradigmatic conjugated polymer, poly(2-methoxy-5-(2-ethylhexyloxy)-1,4-phenylenevinylene) (MEH-PPV). Two equivalent sample films were prepared by spin-casting a toluene solution of MEH-PPV (ca. 0.5 nM) containing 6 wt% host poly(methyl methacrylate) (PMMA) matrix on a QCM sensor and a glass coverslip and placed in the SVA chamber. An acetone–chloroform solvent mixture with liquid volume ratio of 50:50% was employed to swell the films.[2f] We performed SVA for about 55 min to generate and grow aggregates, during which we carefully controlled the extent of film swelling to maintain a constant thickness (Supporting Information, Figure S1a).

---

[*] Dr. J. Yang, Prof. Dr. H. Park, Prof. Dr. L. J. Kaufman
Department of Chemistry, Columbia University
3000 Broadway, New York, NY 10027 (USA)
E-mail: kaufman@chem.columbia.edu
Prof. Dr. H. Park
Department of Physics and Astronomy
Texas A&M University—Commerce
Commerce, TX 75429 (USA)

Supporting information and the ORCID identification number(s) for the author(s) of this article can be found under:
https://doi.org/10.1002/anie.201710336.

With this degree of swelling, individual aggregates could be tracked, localized, and characterized. For in situ optical imaging over the course of aggregate growth, a series of 200 s videos with intervals of 400 s were collected. Additional details can be found in the Methods in the Supporting Information.

First, to characterize time-dependent growth of MEH-PPV aggregates over the duration of film swelling, we assessed change in aggregate size and number by analyzing the average of the first 10 frames in videos recorded every 10 min. Aggregate size was assessed through calculation of number of single chains per aggregate, $N_{\text{SM-AGG}}$ (see Methods in the Supporting Information for details). As depicted in Figure 1, $N_{\text{SM-AGG}}$ increases gradually while number of aggregates decreases. Since the imaging area was different for each video, photobleaching did not contribute to the decrease in aggregate number. Thus, the observed anti-correlation between $N_{\text{SM-AGG}}$ and aggregate number shows that the portion of aggregate growth represented by Figure 1 occurs through mechanisms that consume existing aggregates.

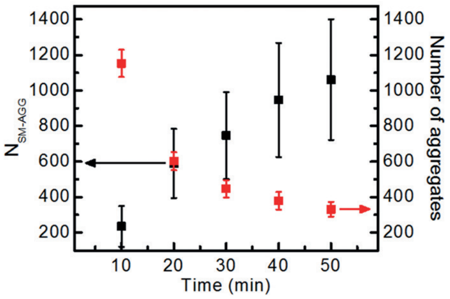

Figure 1. Growth of conjugated polymer aggregates in a swollen film. Average number of single MEH-PPV chains per aggregate, $N_{\text{SM-AGG}}$ (black), and number of aggregates within an imaging volume of about 1400 μm^3 (red) as a function of SVA time.

While the trends depicted in Figure 1 reveal that latter portions of the aggregation process involve consumption of aggregates formed early in the process, in situ tracking of individual diffusing aggregates can provide additional information on the mechanism of aggregate growth. For example, the MEH-PPV aggregate shown in Figure 2 a shows a gradual increase in fluorescence intensity while its diffusivity decreases. The fact that these temporal changes in intensity and diffusivity are anti-correlated suggests that this aggregate is growing. During this aggregate growth process, intensity increases gradually and no overt coalescence of large entities is seen; these observations are consistent with growth through Ostwald ripening, and we presume the observed growth occurs through addition of single chains. If Ostwald ripening is indeed an operative mechanism of aggregate growth, dissipating aggregates should also be in evidence. We do observe aggregates that simultaneously become dimmer and faster, and these typically disappear during the video (Figure 2b), making them challenging to characterize. Nevertheless, we identified several slowly dissipating aggregates that survived the duration of the imaging window. One

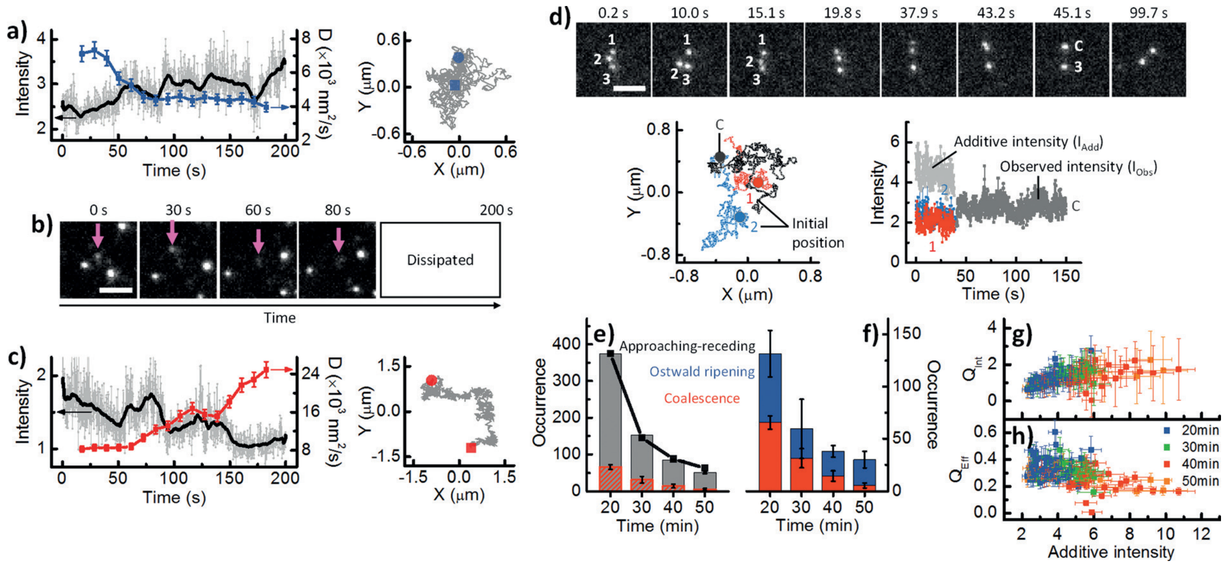

Figure 2. a),c) Fluorescence intensity (gray) and diffusion coefficient (*D*; blue and red) trajectories of MEH-PPV aggregates a) growing and c) dissipating, consistent with an Ostwald ripening growth mechanism. Smoothed intensity trajectories are also shown (black). Shown at right in (a) and (c) are the corresponding trajectories in the *xy* plane for these aggregates. b) Time-lapse fluorescence images showing a typical example of a dissipating aggregate. Scale bar: 2 μm. d) Time-lapse fluorescence images showing approaching-receding (**2** and **3**) and coalescence (**1** and **2**, coalescing to **C**) processes. Scale bar: 2 μm. Shown below are the corresponding trajectories in the *xy* plane and fluorescence intensity trajectories of **1** and **2** before and after (**C**) coalescence. Videos showing aggregates in (a)–(d) are provided in the Supporting Information, Videos S1–S4. All example aggregates shown here were chosen from the video recorded 30 min into SVA. e),f) Frequencies of approaching-receding (gray in e), coalescence (red in e and f), and Ostwald ripening (blue in f) processes over the duration of aggregate tracking videos. In (e), black squares represent $N^2\nu$, normalized to the maximum occurrence of the approaching-receding processes. g),h) Quenched intensity (Q_{Int}; g) and quenching efficiency (Q_{Eff}; h) for aggregates formed by coalescence as functions of additive intensity of two aggregates before coalescence and SVA time. In (a), (c), (d), and (g), intensity units are $\times 10^5$ counts per second.

example is shown in Figure 2c: here, the aggregate shows decreasing intensity with increasing diffusion coefficient, as opposed to the aggregate shown in Figure 2a. The observed dissipation of aggregates is attributed to the Ostwald ripening process as other possibilities, such as photobleaching, aggregate diffusion out of the imaging plane, and out-of-plane aggregate rotation, are excluded (Supporting Information, Text 2). As such, we conclude that the dual observation of growing and dissipating aggregates confirms Ostwald ripening as an operative mechanism in aggregate growth.

Apart from observing the Ostwald ripening process, tracking particular aggregates revealed instances of aggregate coalescence, in which two visualized aggregates merge to form a single larger aggregate (Figure 2d; Supporting Information, Figure S3). Such a mechanism is previously undescribed in the literature of conjugated polymer aggregate growth. In most cases, repetitive approaching-receding events between aggregates were seen, and only a portion of these occurrences led to aggregate coalescence (Figure 2e). Aggregate coalescence occurred over the entire period of swelling once aggregate diffusion was visible by eye: in the video recorded at 10 min into SVA, no coalescence events were seen, presumably since aggregates exhibit low mobility owing to limited film swelling in that time period. Frequency of visualized approaching-receding processes diminished with N^2v, with N number of aggregates and v average aggregate speed, consistent with a second-order process (black squares in Figure 2e).

Both coalescence and Ostwald ripening would give rise to the trends shown in Figure 1, with a decrease in total number of aggregates and increase in number of single molecules per aggregate as a function of aggregate growth time once initial aggregates are formed. To determine how much each growth mechanism contributes to overall aggregate growth, we compared frequency of coalescence and total decrease in aggregate number that occurred over the duration of the videos. Aggregate number decrease was calculated by comparing the number of aggregates in images obtained from averaging the first and last 10 frames in each video. Nearly half of the aggregate number decrease is due to aggregate coalescence (red in Figure 2f), demonstrating the importance of this previously undescribed mechanism in the growth of conjugated polymer aggregates in solvent swollen films. The remainder of aggregate number decrease is attributed to Ostwald ripening (blue in Figure 2f), consistent with the observation of individual dissipating aggregates.

Most of the aggregates formed by coalescence exhibit fluorescence intensities lower than the additive intensity of the two aggregates before coalescence, revealing emergent quenching due to the formation of interchain contacts (Figure 2d). We note that quenching also occurs as aggregates grow through Ostwald ripening (Supporting Information, Text 4). A collection of 145 coalescence events from all aggregate tracking videos reveals a gradual increase of the additive intensity with increasing SVA time, primarily due to increasing aggregate size (from blue to orange in Figure 2g,h). However, quenched intensity, corresponding to the difference between additive and observed intensities ($Q_{\mathrm{Int}} = I_{\mathrm{Add}} - I_{\mathrm{Obs}}$), saturates following a slight increase at early SVA times, resulting in quenching efficiency, $Q_{\mathrm{Eff}} = 1-(I_{\mathrm{Obs}}/I_{\mathrm{Add}})$, decreasing with SVA time (Figure 2g,h). Based on the observed Q_{Int}, the radius of quenching in coalesced aggregates extends approximately 15 nm, suggesting that aggregates most likely experience minimal contact during coalescence, rather than an H-type configuration that would result in substantial surface contact (Supporting Information, Text 5).

We further investigated whether growth mechanism impacted aggregate morphology and photophysical properties through measurements of aggregate polarization modulation depth (M)[5] before and after coalescence events. These measurements were performed in a quasi-real time manner (Supporting Information, Figure S1b): following SVA for 30 min to generate aggregates, sample films were de-swelled and initial M measurements were performed. Solvent vapor was then re-introduced, and when the film was sufficiently swollen such that aggregate diffusion was evident, a long-duration (300 s) video was recorded. Following this, the film was de-swelled and M measurements were performed again. The imaging area was fixed for the entirety of the experiment. Figure 3a shows representative data obtained from coalescing aggregates in this experiment. Here, two aggregates initially exhibit high M values. They coalesce during the film re-swelling process, and the resultant aggregate exhibits a decreased value of $M < 0.5$.

We compared M values before and after coalescence for all such events captured in the long duration movie (Figure 3b). Before, aggregates predominantly exhibit fairly high M values, with median $M = 0.65$ for the distribution, indicating that aggregate morphology is fairly anisotropic. Coalescence events predominantly yield aggregates with lower M values, decreasing the median M to 0.43. While this finding suggests coalescence events attenuate optical (and presumably structural) anisotropy of aggregates, because changes in M values may also emerge from changes in number of emitting dipoles,[5e] complementary Monte Carlo simulations of coalescence were performed.

We modeled a situation in which two aggregates form a minimal contact, a situation that would result in the initial characteristics of each aggregate being nearly the same before and after coalescence. Such a pair of aggregates may be effectively modeled by two equivalent polarization ellipsoids,[2a–f] each with transition dipoles (μ_x, μ_y, μ_z) and an aspect ratio $\alpha = |\mu_z|/|\mu_x|$ ($|\mu_x| = |\mu_y|$), present together within a diffraction-limited spot. Through comparison of aggregate volume and M distribution in experiments and simulation, aggregates before coalescence are determined to have average aspect ratio $\alpha = 2.7$ (Supporting Information, Text 6 and Figure S5). The relative orientation of a pair of such model aggregates is defined by two angles θ and ϕ, as illustrated in Figure 3c. Randomly locating simulated aggregate pairs in 3D space eliminates the ϕ-dependence of the M value. For a situation with individual aggregates with $\alpha = 2.7$ and either $\theta = 50° - 70°$ or θ chosen at random for each aggregate pair, simulated aggregate pairs yield M values that largely reproduced the experimental M distribution after coalescence (Figure 3b; Supporting Information, Text 6 and Figure S6). The consistency of the experimental data with aggregate coalescence occurring with preferential orientation

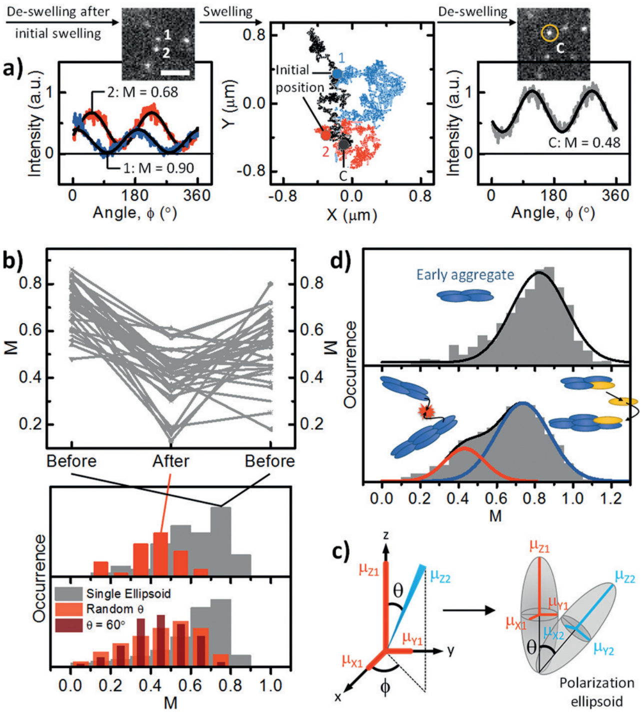

Figure 3. Impact of aggregate growth mechanism on morphological order. a) Fluorescence images and intensity modulation traces with fits of MEH-PPV aggregates (left) before and (right) after coalescence. Scale bar in the images: 2 μm. Shown in the center are trajectories in the *xy* plane of the aggregates shown in the left and right images. Corresponding video is provided in the Supporting Information, Video S5. b) (top) Plot and (middle) histograms showing changes in aggregate *M* values due to coalescence. 32 coalescence events were analyzed. In the bottom panel in (b), gray histogram represents the *M* distribution of simulated aggregates with $\alpha = 2.7$. Dark red and light red histograms represent *M* distributions of 10^7 simulated aggregate pairs, obtained with $\theta = 60°$ and θ chosen randomly. c) Representation illustrating orientation of simulated aggregates presumed to be within a diffraction-limited spot. Angles θ and ϕ are the polar angle between μ_{Z2} and μ_{Z1} and the azimuthal angle between μ_{Z2} projected on the $\mu_{X1}\mu_{Y1}$-plane and μ_{X1}, respectively. d) *M* distributions for aggregates prepared from SVA of sample films for (top) 15 min and (bottom) 55 min, respectively. Also shown are Gaussian and bi-Gaussian fit curves (black). 800 individual aggregates were analyzed and are represented in each distribution. The bi-Gaussian fit was obtained by fixing the center of the fit curve at lower *M* at 0.43, obtained from a Gaussian fit of the experimental results presented in the red histogram in the middle panel of (b).

of $\theta = 50° - 70°$ could be related to steric effects. However, given consistency with randomly distributed θ, in the absence of specific evidence regarding steric effects, we conclude that coalescence likely occurs at random orientation and through minimal contact. This does not attenuate the anisotropy of either of the individual aggregates but suppresses the overall anisotropy of the pair.

We also interrogated morphological order of aggregates grown primarily by Ostwald ripening by comparing *M* values of MEH-PPV aggregates during initial and final stages of growth, with the early aggregates unlikely to have experienced aggregate coalescence since the SVA process was arrested before early aggregates exhibited significant mobility. The *M* values of the early aggregates show a single narrow Gaussian distribution peaked at $M \approx 0.82$ (Figure 3 d, upper), revealing that the morphology of aggregates in the initial growth stages is highly anisotropic. Given that single-molecule MEH-PPV molecules have been shown to adopt highly ordered anisotropic conformations after SVA as evidenced by values of $M > 0.9$,[2f,6] the anisotropic morphology of the early aggregates suggests that initial aggregation processes preserve the morphological anisotropy templated by the single chain building blocks. The *M* distribution for the final aggregates shifts towards lower *M* values and broadens, displaying a population build-up at $M \approx 0.45$ (Figure 3 d, lower). This distribution is well-fit by a bi-Gaussian, in which the distribution centered at the lower *M* value closely matches the *M* distribution for the aggregates formed by coalescence, shown in red in Figure 3 b. The distribution centered at higher *M* is thus attributed to aggregates grown through Ostwald ripening. This, together with the similar *M* distribution seen in early aggregates, reveals that this growth mechanism, in contrast to aggregate coalescence, preserves anisotropic morphology templated at the single molecule and early aggregate level.

In summary, we observed the dynamic growth of MEH-PPV aggregates in swollen polymer films by performing in situ optical imaging with simultaneous control of film swelling properties. Aggregate growth is found to proceed through two mechanisms: classical Ostwald ripening as well as the previously undescribed concerted mechanism of diffusing aggregate coalescence. Aggregate growth via Ostwald ripening preserves the high degree of morphological ordering templated by single molecules while aggregate coalescence occurs without directionality, typically leading to attenuation of the degree of ordering as the aggregates grow. This suggests that by limiting conditions that favor coalescence processes, such as a high degree of swelling that encourages early aggregate diffusion, one may be able to prepare large aggregates with a high degree of morphological anisotropy that in turn supports desirable photophysical properties such as long-range exciton diffusion.

Acknowledgements

This work was supported in part by the National Science Foundation under grant CHE1660392.

Conflict of interest

The authors declare no conflict of interest.

Keywords: coalescence · conjugated polymer aggregates · in situ optical imaging · morphology · Ostwald ripening

How to cite: *Angew. Chem. Int. Ed.* **2018**, *57*, 1826–1830
Angew. Chem. **2018**, *130*, 1844–1848

---

[1] a) H. N. Tsao, K. Mullen, *Chem. Soc. Rev.* **2010**, *39*, 2372–2386; b) R. Noriega, J. Rivnay, K. Vandewal, F. P. V. Koch, N. Stingelin,

P. Smith, M. F. Toney, A. Salleo, *Nat. Mater.* **2013**, *12*, 1038 – 1044; c) S. D. Kang, G. J. Snyder, *Nat. Mater.* **2017**, *16*, 252 – 257; d) A. Neff, F. Niefind, B. Abel, S. C. B. Mannsfeld, K. R. Siefermann, *Adv. Mater.* **2017**, *29*, 1701012; e) R. J. Kline, M. D. McGehee, *Polym. Rev.* **2006**, *46*, 27 – 45; f) X. N. Yang, J. Loos, S. C. Veenstra, W. J. H. Verhees, M. M. Wienk, J. M. Kroon, M. A. J. Michels, R. A. J. Janssen, *Nano Lett.* **2005**, *5*, 579 – 583; g) E. Moons, *J. Phys. Condens. Matter* **2002**, *14*, 12235 – 12260; h) T. Q. Nguyen, R. C. Kwong, M. E. Thompson, B. J. Schwartz, *Appl. Phys. Lett.* **2000**, *76*, 2454 – 2456.

[2] a) J. Vogelsang, T. Adachi, J. Brazard, D. A. Vanden Bout, P. F. Barbara, *Nat. Mater.* **2011**, *10*, 942 – 946; b) J. Vogelsang, J. M. Lupton, *J. Phys. Chem. Lett.* **2012**, *3*, 1503 – 1513; c) M. C. Traub, J. Vogelsang, K. N. Plunkett, C. Nuckolls, P. F. Barbara, D. A. Vanden Bout, *ACS Nano* **2012**, *6*, 523 – 529; d) Z. J. Hu, T. Adachi, R. Haws, B. Shuang, R. J. Ono, C. W. Bielawski, C. F. Landes, P. J. Rossky, D. A. Vanden Bout, *J. Am. Chem. Soc.* **2014**, *136*, 16023 – 16031; e) T. Stangl, P. Wilhelm, K. Remmerssen, S. Hoger, J. Vogelsang, J. M. Lupton, *Proc. Natl. Acad. Sci. USA* **2015**, *112*, 5560 – 5566; f) J. Yang, H. Park, L. J. Kaufman, *J. Phys. Chem. C* **2017**, *121*, 13854 – 13862; g) Z. J. Hu, R. T. Haws, Z. P. Fei, P. Boufflet, M. Heeney, P. J. Rossky, D. A. Vanden Bout, *Proc. Natl. Acad. Sci. USA* **2017**, *114*, 5113 – 5118; h) F. Steiner, J. M. Lupton, J. Vogelsang, *J. Am. Chem. Soc.* **2017**, *139*, 9787 – 9790; i) D. Würsch, F. J. Hofmann, T. Eder, A. V. Aggarwal, A. Idelson, S. Hoger, J. M. Lupton, J. Vogelsang, *J. Phys. Chem. Lett.* **2016**, *7*, 4451 – 4457; j) D. T. Hoang, J. Yang, K. Paeng, Y. Kwon, O. S. Kweon, L. J. Kaufman, *Rev. Sci. Instrum.* **2016**, *87*, 015106.

[3] a) I. M. Lifshitz, V. V. Slyozov, *J. Phys. Chem. Solids* **1961**, *19*, 35 – 50; b) M. Kahlweit, *Adv. Colloid Interface Sci.* **1975**, *5*, 1 – 35.

[4] a) N. T. K. Thanh, N. Maclean, S. Mahiddine, *Chem. Rev.* **2014**, *114*, 7610 – 7630; b) M. A. Boles, M. Engel, D. V. Talapin, *Chem. Rev.* **2016**, *116*, 11220 – 11289.

[5] a) D. H. Hu, J. Yu, K. Wong, B. Bagchi, P. J. Rossky, P. F. Barbara, *Nature* **2000**, *405*, 1030 – 1033; b) O. Mirzov, R. Bloem, P. R. Hania, D. Thomsson, H. Z. Lin, I. G. Scheblykin, *Small* **2009**, *5*, 1877 – 1888; c) S. Furumaki, S. Habuchi, M. Vacha, *Chem. Phys. Lett.* **2010**, *487*, 312 – 314; d) T. Adachi, J. Brazard, P. Chokshi, J. C. Bolinger, V. Ganesan, P. F. Barbara, *J. Phys. Chem. C* **2010**, *114*, 20896 – 20902; e) H. Park, D. T. Hoang, K. Paeng, J. Yang, L. J. Kaufman, *Nano Lett.* **2015**, *15*, 7604 – 7609; f) P. Wilhelm, J. Vogelsang, G. Poluektov, N. Schonfelder, T. J. Keller, S. S. Jester, S. Hoger, J. M. Lupton, *Angew. Chem. Int. Ed.* **2017**, *56*, 1234 – 1238; *Angew. Chem.* **2017**, *129*, 1254 – 1258; g) H. Piwonski, T. Michinobu, S. Habuchi, *Nat. Commun.* **2017**, *8*, 15256; h) S. H. Lee, J. Yang, D. Kim, *J. Phys. Chem. Lett.* **2016**, *7*, 3676 – 3682; i) R. Camacho, S. Tubasum, J. Southall, R. J. Cogdell, G. Sforazzini, H. L. Anderson, T. Pullerits, I. G. Scheblykin, *Sci. Rep.* **2015**, *5*, 15080.

[6] J. Vogelsang, J. Brazard, T. Adachi, J. C. Bolinger, P. F. Barbara, *Angew. Chem. Int. Ed.* **2011**, *50*, 2257 – 2261; *Angew. Chem.* **2011**, *123*, 2305 – 2309.

Manuscript received: October 6, 2017
Revised manuscript received: December 2, 2017
Accepted manuscript online: December 27, 2017
Version of record online: January 24, 2018